

Origin of hibonite-pyroxene spherules found in carbonaceous chondrites

STEVEN B. SIMON^{1*}, ANDREW M. DAVIS², LAWRENCE GROSSMAN^{1,2} AND ERNST K. ZINNER³

¹Department of the Geophysical Sciences, The University of Chicago, 5734 South Ellis Avenue, Chicago, Illinois 60637, USA

²Enrico Fermi Institute, The University of Chicago, 5640 South Ellis Avenue, Chicago, Illinois 60637, USA

³McDonnell Center for the Space Sciences and Physics Department, Washington University, St. Louis, Missouri 63130, USA

*Correspondence author's e-mail address: sbs8@midway.uchicago.edu

(Received 1997 April 14; accepted in revised form 1998 January 6)

Abstract—We have studied both of the known glass-free, hibonite-pyroxene spherules: MYSM3, from Murray (CM2), and Y17-6, from Yamato 791717 (CO3). They consist of hibonite plates (~2 wt% $\text{TiO}_2^{\text{tot}}$) enclosed in Al-rich pyroxene that has such high amounts of CaTs ($\text{CaAl}_2\text{SiO}_6$) component, up to ~80 mol%, that it must have crystallized metastably. Within the pyroxene, abundances of MgO and SiO_2 are strongly correlated with each other and are anticorrelated with those of Al_2O_3 , reflecting an anticorrelation between the diopside and CaTs components of the pyroxene. In contrast with previous results for Type B fassaite, however, we do not observe an anticorrelation between MgO and $\text{TiO}_2^{\text{tot}}$, possibly reflecting different relative distribution coefficients for Ti^{3+} and Ti^{4+} in the aluminous pyroxene of the spherules from those found for fassaite in Type B inclusions. Previously described hibonite-silicate spherules have ^{26}Mg deficits but the present samples do not. Furthermore, the pyroxene in Y17-6 has excess ^{26}Mg , while the hibonite it encloses does not, indicating that the two phases either had different initial $^{26}\text{Al}/^{27}\text{Al}$ ratios or different initial $^{26}\text{Mg}/^{24}\text{Mg}$ ratios. The Ti isotopic compositions of the present samples are highly unusual: $\delta^{50}\text{Ti} = 103.4 \pm 5.2\%$ in MYSM3 and $-61.4 \pm 4.1\%$ in Y17-6, which are among the largest ^{50}Ti anomalies reported for any refractory inclusion. The textures suggest that hibonite crystallized first; but based on the calculated bulk compositions of both spherules, it is not the liquidus phase in either sample, which suggests that the hibonite in both samples is relict. The presence of ragged hibonite grains in MYSM3 and rounded hibonite grains in Y17-6 and a lack of isotopic equilibrium between pyroxene and hibonite support this conclusion. The spherules crystallized from liquid droplets that probably formed as a result of the melting of solid precursor grains that included hibonite. The heating events were too short and/or not hot enough to melt all the hibonite. The droplets cooled quickly enough that CaTs-rich pyroxene crystallized instead of anorthite. Based on the observed differences in isotopic composition, it is unlikely that the precursors of the present samples formed in the same reservoir as each other or as the previously described hibonite-silicate spherules, providing further evidence of the isotopic heterogeneity of the early solar nebula.

INTRODUCTION

Hibonite is one of the most refractory minerals found in meteorites. It is second only to corundum in the sequence of phases predicted to condense at equilibrium from a gas of solar composition at total pressures $< 1 \times 10^{-2}$ atm (Yoneda and Grossman, 1995). Hibonite takes up rare earth elements and is commonly a carrier of isotopic anomalies. These features make hibonite a potentially powerful recorder of physico-chemical conditions and processes in the very early stages of the solar system and, therefore, all types of hibonite-bearing refractory inclusions are important.

Probably the most common hibonite-bearing inclusions are the silica-poor, spinel-hibonite spherules found in CM2 chondrites (e.g., Macdougall, 1981; MacPherson *et al.*, 1983; Simon *et al.*, 1994). Much less common are spherules in which hibonite laths are enclosed in a silicate. Hibonite-glass spherules have been found in the CH chondrite ALH 85085 (Grossman *et al.*, 1988; MacPherson *et al.*, 1989), the CO3 chondrite Lancé (Kurat, 1975; Ireland *et al.*, 1991), and the Murchison CM2 chondrite (Ireland *et al.*, 1991). Spherules with hibonite laths enclosed in a pyroxene-glass intergrowth have been reported from the CO3 chondrites Colony and ALH 82101 (Russell *et al.*, 1998). In addition to their mineralogy, most hibonite-glass spherules are unusual in that they tend to have ^{26}Mg deficits relative to terrestrial values. These deficits are not well understood. Ireland *et al.* (1991) favor very early formation; while Russell *et al.* (1998) also favor either very early formation, prior to ^{26}Al addition to the solar nebula, or isotopic heterogeneity

in the early solar nebula as possible explanations of the ^{26}Mg deficits. The hibonite-glass spherules in ALH 85085 also have small deficits in ^{26}Mg that are not correlated with Al/Mg (MacPherson *et al.*, 1989; A. M. Davis, unpublished data).

Through freeze-thaw disaggregation of the Murray (CM2) carbonaceous chondrite, we have found a sample of one of these rare types of hibonite-bearing inclusions: a hibonite-pyroxene spherule. Only one other hibonite-pyroxene spherule is known, in a thin section of Yamato 791717, a CO3 chondrite (Tomeoka *et al.*, 1992). We have studied both of these spherules and report here the first petrologic, trace element and isotopic data for this type of inclusion. We use these results to determine whether they contain relict hibonite and to determine whether these spherules are related to the hibonite-glass spherules. Some preliminary findings of this study were reported by Simon *et al.* (1993, 1997a).

ANALYTICAL METHODS

The Murray spherule, MYSM3, was recovered by handpicking from the high-density ($\rho > 3.5$) separate obtained from the products of freeze-thaw disaggregation of a bulk sample following the method of MacPherson *et al.* (1980). Polished thin sections of both (Murray and Yamato) spherules were examined with a JEOL JSM-5800LV scanning electron microscope equipped with an Oxford/Link ISIS-300 energy-dispersive x-ray microanalysis system. Quantitative wavelength-dispersive mineral analyses were obtained with a Cameca SX-50 electron microprobe operated at 15 kV with a beam current of 40 nA. Data were reduced *via* the modified ZAF

correction procedure PAP (Pouchou and Pichoir, 1984). Using an LIF crystal, the interference from the $\text{TiK}\beta$ peak at the wavelength of $\text{VK}\alpha$ is small. Analyses of our V-free, pure TiO_2 standard typically give ~ 0.2 wt% V_2O_5 , so in the present samples, with ≤ 5 wt% TiO_2 , the effect of Ti interference on V is negligible.

Trace element and Mg isotopic analyses were obtained using the University of Chicago AEI IM-20 ion microprobe. The analytical techniques used are similar to those described in Simon *et al.* (1991) and MacPherson and Davis (1993, 1994).

The ^{50}Ti anomalies in the spherules are so large that they could be determined from the trace element scans. The data were corrected for isobaric interferences from Mg_2^+ , SiO^+ , Ca^+ , V^+ and Cr^+ and normalized to ^{48}Ti . No significant corrections had to be made to mass 47; corrections to mass 48 were 20–67‰ for $^{48}\text{Ca}^+$ and $<1\%$ for Mg_2^+ ; corrections to mass 49 were 0–2‰ for Mg_2^+ ; and corrections to mass 50 were 1–4‰ for $^{50}\text{V}^+$, 6–10‰ for $^{50}\text{Cr}^+$ and 0–2‰ for Mg_2^+ . Analyses of a number of isotopically normal samples gave $\Delta^{47}\text{Ti}$, $\Delta^{49}\text{Ti}$ and $\Delta^{50}\text{Ti}$ values within 2σ of normal. This observation, coupled with the near normal $\Delta^{47}\text{Ti}$ and $\Delta^{49}\text{Ti}$ values in the hibonite-pyroxene spherules, gives us confidence that all of the corrections for isobaric interferences were done properly and that there was no instrumental mass fractionation within the precision of $\pm 7\text{‰/amu}$ under the energy filtering conditions used for trace element analysis. These results (for ^{50}Ti) were reported by Simon *et al.* (1997a). Because this method is unorthodox, yielded fairly large uncertainties due to poor counting statistics, and because Ca isotopes could not be measured with the Chicago ion probe, isotopic compositions of Ca and Ti were determined with the modified Cameca IMS-3f ion microprobe at Washington University. The same analysis technique as that described by Zinner *et al.* (1986) and Ireland (1990) was used. The data are normalized to terrestrial $^{40}\text{Ca}/^{44}\text{Ca}$ and $^{46}\text{Ti}/^{48}\text{Ti}$ ratios assuming an exponential mass fractionation law. Corrections for interferences from ^{48}Ti , ^{46}Ca , ^{50}V and ^{50}Cr were made during the measurement runs. Interferences from Sr^{++} to the ^{43}Ca and ^{44}Ca signals and contribution of the tail of ^{48}Ca to the ^{48}Ti signal were negligible.

RESULTS

Petrography

Prior to sectioning, MYSM3 appeared to be a pale blue, diamond-shaped object. In thin section, it is seen to be a spherule in transmitted light, $70\text{ }\mu\text{m}$ across, containing two colorless, anhedral pyroxene grains with nearly uniform extinction. Both grains are $70 \times 35\text{ }\mu\text{m}$ in size. They enclose smaller, subhedral grains of hibonite, also colorless. In a backscattered electron (BSE) image, Fig. 1a, the hibonite plates, seen edge-on, are $\sim 10\text{ }\mu\text{m}$ thick and $\sim 20\text{ }\mu\text{m}$ long. Two grains occur near the edge of the spherule and the others are in the interior. Most have irregular, jagged ends. Two examples are indicated by arrows. These grains are reminiscent of broken crystals that might be found in a breccia. On the other hand, pyroxene/pyroxene contacts are straight and smooth. The outermost margins of the pyroxene grains at the edge of the spherule are smooth and rounded except where they are in contact with a porous, 1–10 μm thick layer of forsterite. The pyroxene/forsterite contacts are either straight or serrated. The forsterite encloses a NiFe grain that is $\sim 1\text{ }\mu\text{m}$ across.

The Yamato spherule, Y17-6 of Tomeoka *et al.* (1992), is present in a polished thin section of the host meteorite, Yamato 791717. The spherule (Fig. 1b) is $120\text{ }\mu\text{m}$ across and contains two colorless, anhedral pyroxene grains with uniform extinction. One grain is semicircular, $100 \times 70\text{ }\mu\text{m}$, and composes about half of the spherule. The other is tabular and smaller ($60 \times 20\text{ }\mu\text{m}$). Each partially to

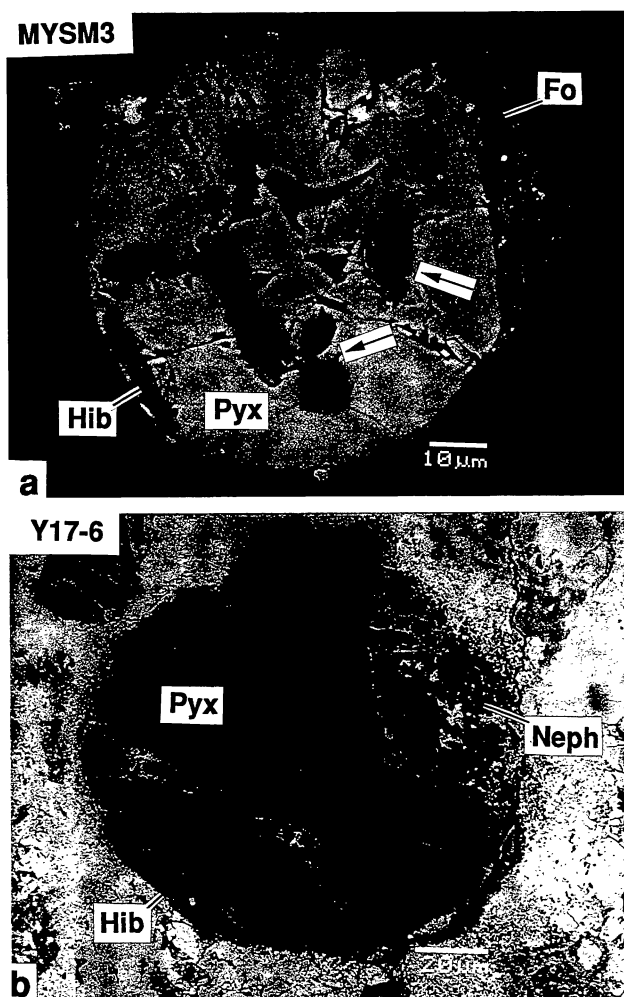


FIG. 1. Backscattered electron images of hibonite-pyroxene spherules. (a) Murray spherule MYSM3. Arrows point to jagged edges of hibonite crystals. (b) Yamato spherule Y17-6, from meteorite Yamato 791717. Pyx = pyroxene. Hib = hibonite. Fo = forsterite. Neph = nepheline.

completely encloses several colorless hibonite grains, which are euhedral to rounded plates, $\sim 20\text{ }\mu\text{m}$ across. Some are seen edge-on and are 5–10 μm thick and up to 40 μm long. Most of the hibonite is at or near the edge of the spherule, with only two grains in the interior. Nepheline, a secondary alteration product, occurs in a crack and in a single, large, continuous area that completes the spherical outline of the inclusion. A hibonite plate crosses the nepheline-filled vein but was not altered, which suggests that only pyroxene, and not hibonite, was converted to nepheline.

Mineral Chemistry

Pyroxene—The pyroxene in the spherules is predominantly a solid solution of diopside (Di; $\text{CaMgSi}_2\text{O}_6$) and Ca-Tschermak's molecule (CaTs; $\text{CaAl}_2\text{SiO}_6$), with a minor Ti-pyroxene (Tpx; $\text{CaTiAl}_2\text{O}_6$) component. Although some Ti probably occurs as Ti^{3+} , we report all Ti as Ti^{4+} (or as $\text{TiO}_2^{\text{tot}}$) because the Ti contents of both pyroxene and hibonite are too low for accurate calculation of $\text{Ti}^{3+}/\text{Ti}^{4+}$ ratios.

The x-ray maps of the distribution of Mg, Al, Si and Ti in the spherules are shown in Fig. 2. The maps of MYSM3 (Figs. 2a–d) show that Mg and Si are strongly correlated with each other and are anticorrelated with Al. These relationships are also observed

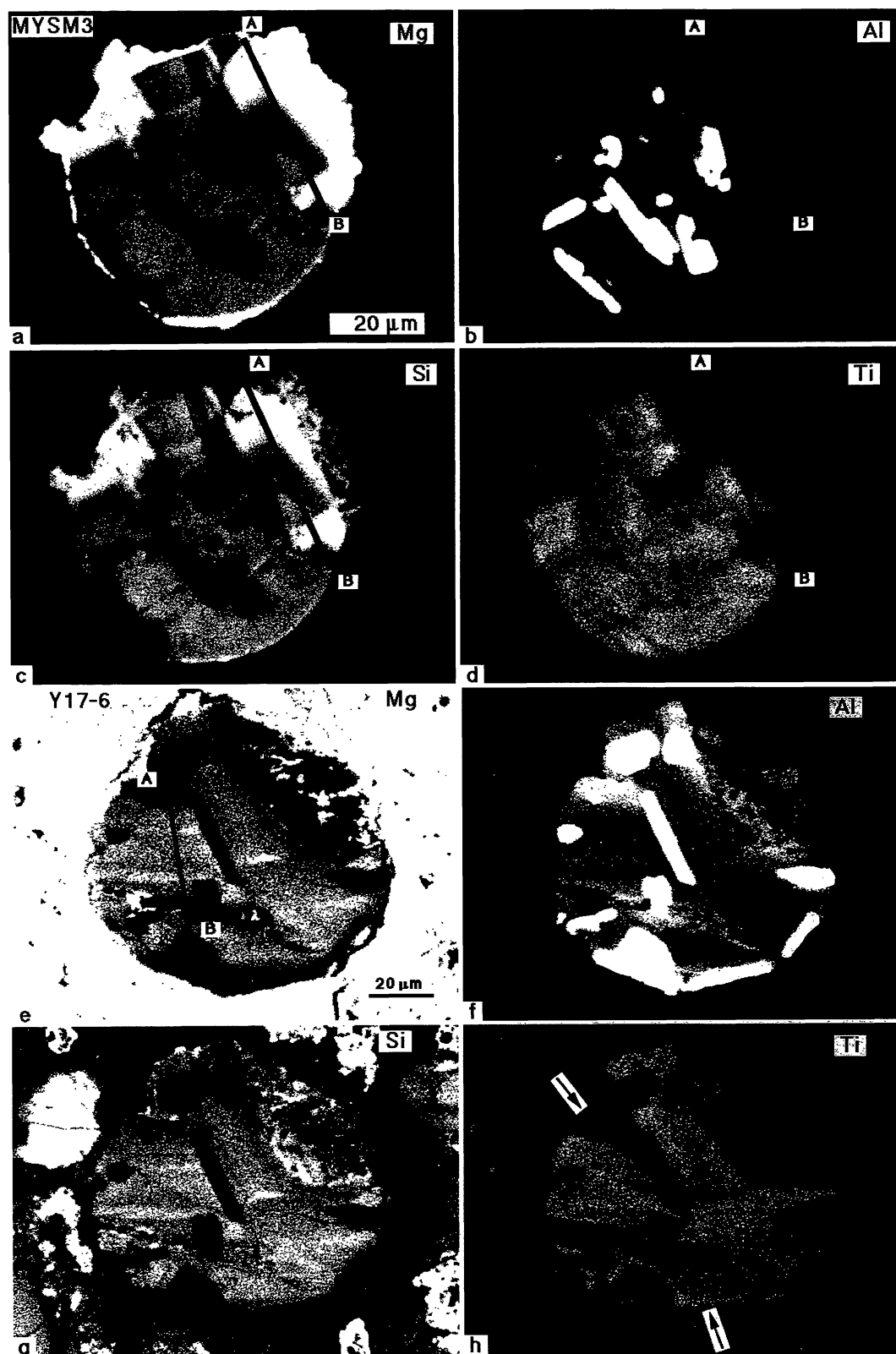


FIG. 2. Energy-dispersive x-ray maps of the spherules. Note strong zoning in MYSM3, in contrast with Y17-6. Forsterite and diopside-rich pyroxene are not visible in the Al and Ti maps. (a) Mg in MYSM3. Line AB is the location of the electron probe traverse discussed in the text and is shown in a–d as a reference point. (b) Al in MYSM3. (c) Si in MYSM3. (d) Ti in MYSM3. (e) Mg in Y17-6. Line AB is the location of the electron probe traverse discussed in the text. (f) Al in Y17-6. (g) Si in Y17-6. (h) Ti in Y17-6. Arrows indicate features discussed in the text.

in fassaite from Allende Type B refractory inclusions (Simon *et al.*, 1991). Abundances of $\text{TiO}_2^{\text{tot}}$ in the pyroxene are fairly uniform, except in several places near the edge of the spherule where the pyroxene is very Di (Mg, Si)-rich and Ti-poor. These regions are dark in Fig. 2d. Fassaite that is relatively SiO_2 -rich and $\text{TiO}_2^{\text{tot}}$ -poor is typically texturally late in Type B inclusions (Simon *et al.*, 1991). Therefore, it is somewhat curious that, in MYSM3, the most SiO_2 -rich, $\text{TiO}_2^{\text{tot}}$ -poor pyroxene found in the sample occurs at the edge where the earliest pyroxene might be expected to form, if the spherule formed by crystallization of a molten droplet from the outside in.

Analyses of typical, Al-rich, and Si-rich pyroxene from MYSM3 are given in columns 1–3, respectively, of Table 1. Overall in the inclusion, pyroxene compositions range from SiO_2 -poor (~30 wt% SiO_2) and very aluminous (~40 wt% Al_2O_3) to aluminous diopside with ~9 wt% Al_2O_3 and ~50 wt% SiO_2 . Abundances of $\text{TiO}_2^{\text{tot}}$ in MYSM3 pyroxene range from below the detection limit of the electron probe (0.036 wt%) to ~4 wt%. An electron probe traverse across an optically continuous, strongly zoned region of MYSM3 (A–B in Fig. 2a) exhibits nearly the entire range of pyroxene compositions observed in the sample. The traverse, summarized in Fig. 3, begins in Si-, Mg-rich, Al-, Ti-poor pyroxene. The strong correlation of MgO with SiO_2 and the anticorrelation between these oxides and Al_2O_3 and $\text{TiO}_2^{\text{tot}}$ are clear from Fig. 3.

The x-ray maps of spherule Y17-6 (Figs. 2e–h) show that it has, in contrast to MYSM3, mostly small variations in, and no large-scale zoning with respect to, MgO, Al_2O_3 , and SiO_2 abundances in pyroxene. The Ti x-ray map (Fig. 2h) shows that some of the py-

roxene that is adjacent to hibonite is enriched in $\text{TiO}_2^{\text{tot}}$ relative to that elsewhere in the inclusion. One such location is indicated by the arrow at the bottom of Fig. 2h. Note that, in Y17-6, the hibonite has lower $\text{TiO}_2^{\text{tot}}$ contents than the host pyroxenes; whereas, in MYSM3, the hibonite and the pyroxene adjacent to it have similar $\text{TiO}_2^{\text{tot}}$ contents, and the two phases are indistinguishable in the Ti x-ray map of the sample (Fig. 2d). The Ti-poor pyroxene in MYSM3 is very dark in Fig. 2d.

TABLE 1. Electron microprobe analyses of pyroxene.

	(1)	(2)	(3)	(4)	(5)	(6)
MgO	7.02	2.72	14.38	6.07	3.16	9.04
Al_2O_3	27.20	39.38	9.41	29.16	37.67	21.08
SiO_2	37.09	30.56	49.10	34.75	31.30	40.47
CaO	25.93	25.75	26.15	25.45	25.64	26.10
Cr_2O_3	0.06	0.04	0.04	0.09	0.05	0.04
$\text{TiO}_2^{\text{tot}}$	2.40	1.14	0.04	3.63	1.41	2.26
V_2O_5	0.25	BLD	0.07	0.38	BLD	0.24
FeO	BLD	BLD	0.10	0.56	0.25	0.13
Total	99.95	99.59	99.29	100.09	99.48	99.36
Cations per six oxygen anions						
Si	1.352	1.117	1.790	1.272	1.147	1.485
IVAl	0.648	0.883	0.210	0.728	0.853	0.515
VIAl	0.521	0.814	0.195	0.531	0.773	0.397
Mg	0.381	0.148	0.781	0.331	0.173	0.495
Ca	1.013	1.008	1.022	0.998	1.006	1.026
Cr	0.002	0.001	0.001	0.003	0.002	0.001
Ti	0.066	0.031	0.001	0.100	0.039	0.062
V	0.007	0.0	0.002	0.011	0.0	0.007
Fe	0.0	0.0	0.003	0.017	0.008	0.004
Total	3.990	4.002	4.005	3.991	4.001	3.992
Di	39.4	14.9	79.9	34.4	17.6	51.9
CaTs	53.8	82.0	20.0	55.2	78.5	41.6
Tpx	6.8	3.1	0.1	10.4	3.9	6.5

References: (1) MYSM3, representative analysis. (2) MYSM3, Al-rich pyx. (3) MYSM3, Si-, Mg-rich pyx. (4) Y17-6, representative analysis. (5) Y17-6, Al-rich pyx. (6) Y17-6, Si-, Mg-rich pyx.

BLD = below limit of detection of electron microprobe of 0.024 wt% for V_2O_5 or 0.031 wt% for FeO. All of these analyses have Sc_2O_3 contents below the detection limit of 0.032 wt%.

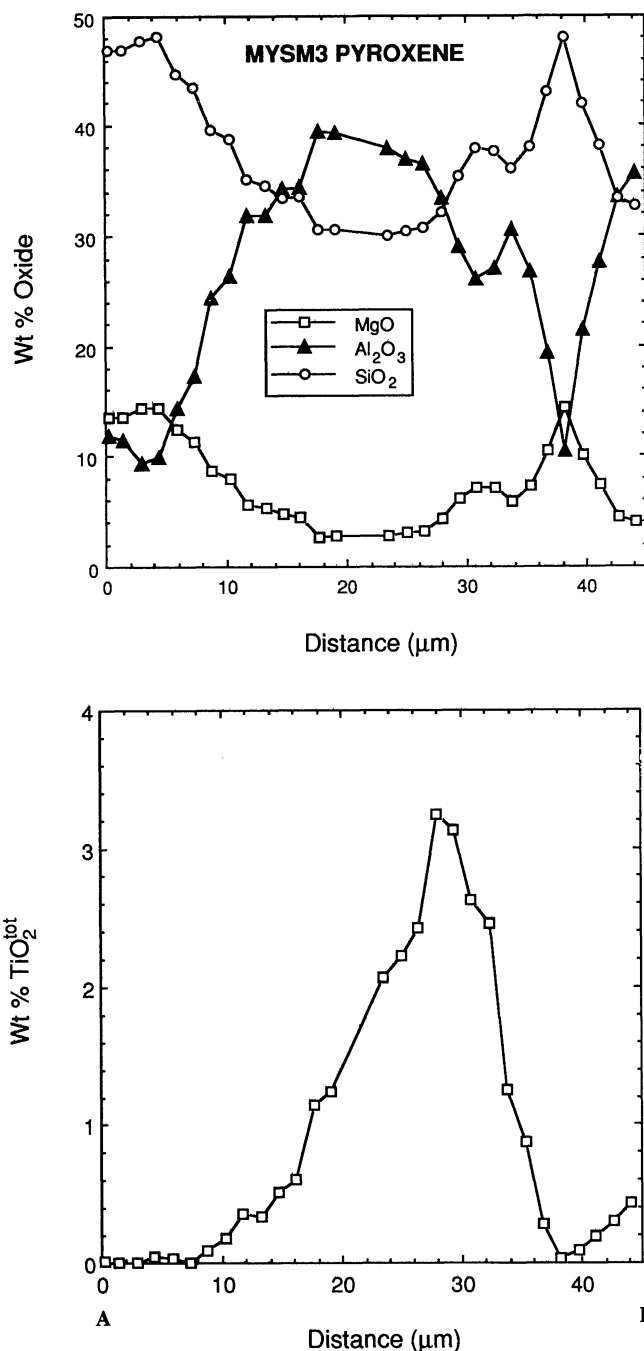


FIG. 3. Results of an electron probe traverse across strongly zoned pyroxene in MYSM3. Location is indicated in Fig. 2a. The Di (MgO, SiO_2) component is strongly anticorrelated with Al_2O_3 and $\text{TiO}_2^{\text{tot}}$.

The Ti map of Y17-6 also shows one small area of pyroxene, indicated by the arrow at the upper left edge of the spherule in Fig. 2h, that has less Ti than the pyroxene elsewhere in the spherule. It is also low in SiO_2 and MgO and is enriched in Al_2O_3 relative to the rest of the pyroxene. The path of an electron probe traverse that starts in this zone and continues across the inclusion is indicated in Fig. 2e. The results (Fig. 4) show some very unusual features. Over the first 15 μm of the traverse, Al_2O_3 decreases sharply and MgO, SiO_2 , and $\text{TiO}_2^{\text{tot}}$ increase. In typical fassaite, $\text{TiO}_2^{\text{tot}}$ is anticorrelated with MgO and SiO_2 (Simon *et al.*, 1991), as is the case in the next 25 μm of this traverse and in the MYSM3 traverse. The behavior changes again, however, as the three oxides covary over the remainder of the traverse, all generally decreasing while Al_2O_3 increases. The places where $\text{TiO}_2^{\text{tot}}$ is correlated with MgO (and SiO_2) are relatively Al-rich areas. In two other traverses across Y17-6, $\text{TiO}_2^{\text{tot}}$ is uncorrelated or anticorrelated with MgO and SiO_2 .

Analyses of typical, Al-rich, and Si-rich pyroxene from Y17-6 are given in columns 4–6, respectively, of Table 1. Contents of SiO_2 , Al_2O_3 and MgO in pyroxene in Y17-6 fall within the ranges observed for the Murray pyroxene. Most of the present analyses are similar to the one previously reported from this inclusion by Tomeoka *et al.* (1992). The Y17-6 pyroxene tends to have higher $\text{TiO}_2^{\text{tot}}$ and V_2O_5 contents than the pyroxene in MYSM3. In several places in Y17-6, $\text{TiO}_2^{\text{tot}}$ contents of pyroxene adjacent to hibonite are 1–2 wt% higher than they are further away. The Al-rich, Ti-poor compositions of most of the pyroxene in these spherules are similar to the compositions of the pyroxene-glass intergrowth in the spherules studied by Russell *et al.* (1998) and are similar to those of the glass in the hibonite-glass spherules studied by Ireland *et al.* (1991).

The narrower range of pyroxene compositions in Y17-6 relative to that observed in MYSM3 is illustrated in Fig. 5 in which data from both of these samples are plotted along with analyses of fassaite from four Allende Type B inclusions (three B1s and one B2) and glasses from the hibonite-glass spherules studied by Ireland *et al.* (1991). The strong correlation of MgO with SiO_2 , due to the coupling of Mg and Si in the Di component of the pyroxene, is evident in Fig. 5a. The trend of the spherule pyroxene extends to much lower MgO and SiO_2 contents and to much higher Al_2O_3 contents (Fig. 5b) than the fassaite from Type B inclusions. The spherule pyroxenes are dominated by their Di and CaTs components, basically plotting on a mixing line between the two, with small additional Tpx components. Fassaite from Type B inclusions has much larger Tpx (both Ti^{3+} and Ti^{4+} end-members) contents than the spherule pyroxene. Among the Type B fassaite analyses, decreasing SiO_2 contents correspond to increasing $\text{TiO}_2^{\text{tot}}$; so, as SiO_2 decreases (Fig. 5b), the Type B trend increasingly diverges from the Di-CaTs trend of the spherules. The dramatic difference between the pyroxene in the spherules and that in Type B inclusions is even more evident in Fig. 5c, a plot of MgO vs. $\text{TiO}_2^{\text{tot}}$. In many pyroxene analyses from the spherules, MgO and $\text{TiO}_2^{\text{tot}}$ contents are much lower than in typical fassaite from Type B inclusions. Also, the spherule analyses do not define a strong negative trend like the one seen for the Type B fassaite in Fig. 5c. The latter pyroxene has $\text{Ti}^{3+}/(\text{Ti}^{3+} + \text{Ti}^{4+})$ ratios that are typically >0.5 and range up to ~ 0.85 (Simon *et al.*, 1991).

In Type B inclusions, the fassaite/liquid distribution coefficient (D) for Ti^{3+} is ~ 3 and that for Ti^{4+} is ~ 1 (Beckett, 1986; Simon *et al.*, 1991). Because most of the Ti in the Type B fassaite is trivalent, the crystals are zoned with Ti-rich cores and Ti-poor rims; and

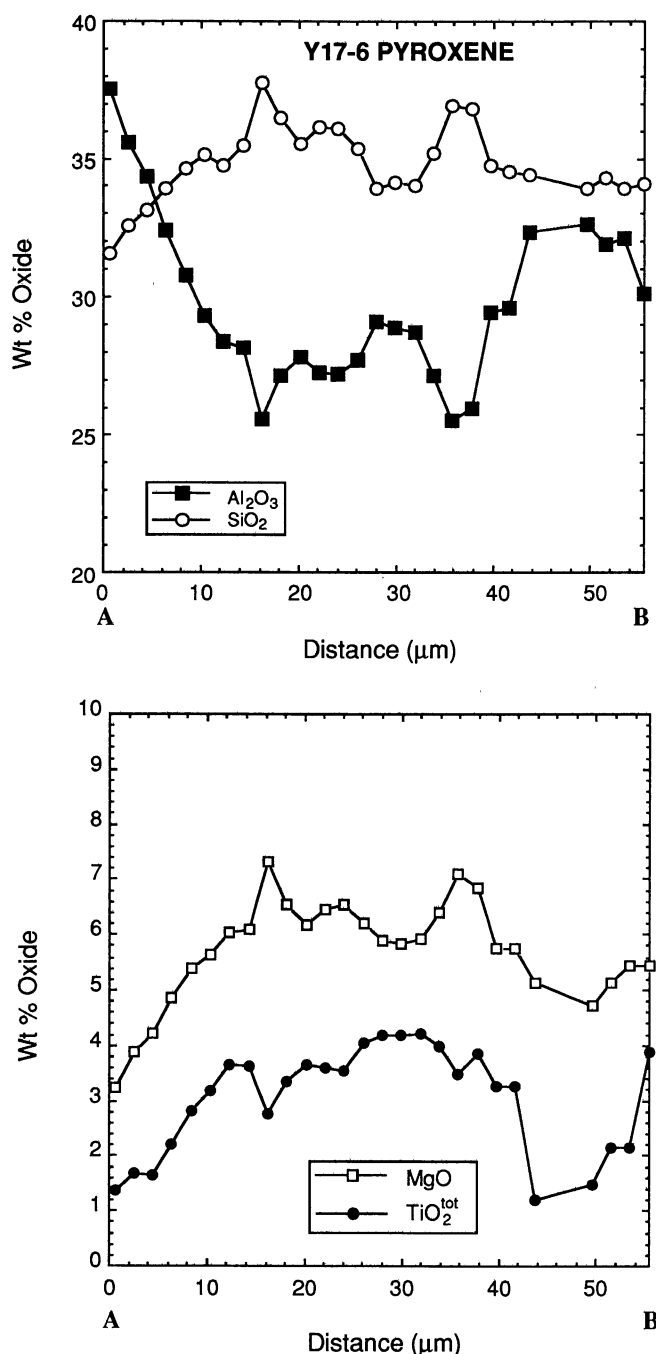


FIG. 4. Results of an electron probe traverse across pyroxene in Y17-6. Location is indicated in Fig. 2e. Note the unusual positive correlation of MgO and $\text{TiO}_2^{\text{tot}}$ over parts of the traverse. The MgO and SiO_2 are positively correlated throughout.

the interelement relationships, such as the $\text{MgO}-\text{TiO}_2^{\text{tot}}$ trend, reflect the behavior of Ti as a strongly compatible element. In contrast, the lack of a well-defined $\text{MgO}-\text{TiO}_2^{\text{tot}}$ trend among the spherule pyroxene analyses indicates that Ti did not strongly partition into this pyroxene, which is consistent with a $D \sim 1$. If the Ds for Ti^{3+} and Ti^{4+} in the spherules were like those found for Type B inclusions, this observation would imply a very low $\text{Ti}^{3+}/\text{Ti}^{4+}$ ratio, which would require an f_{O_2} higher than that inferred for

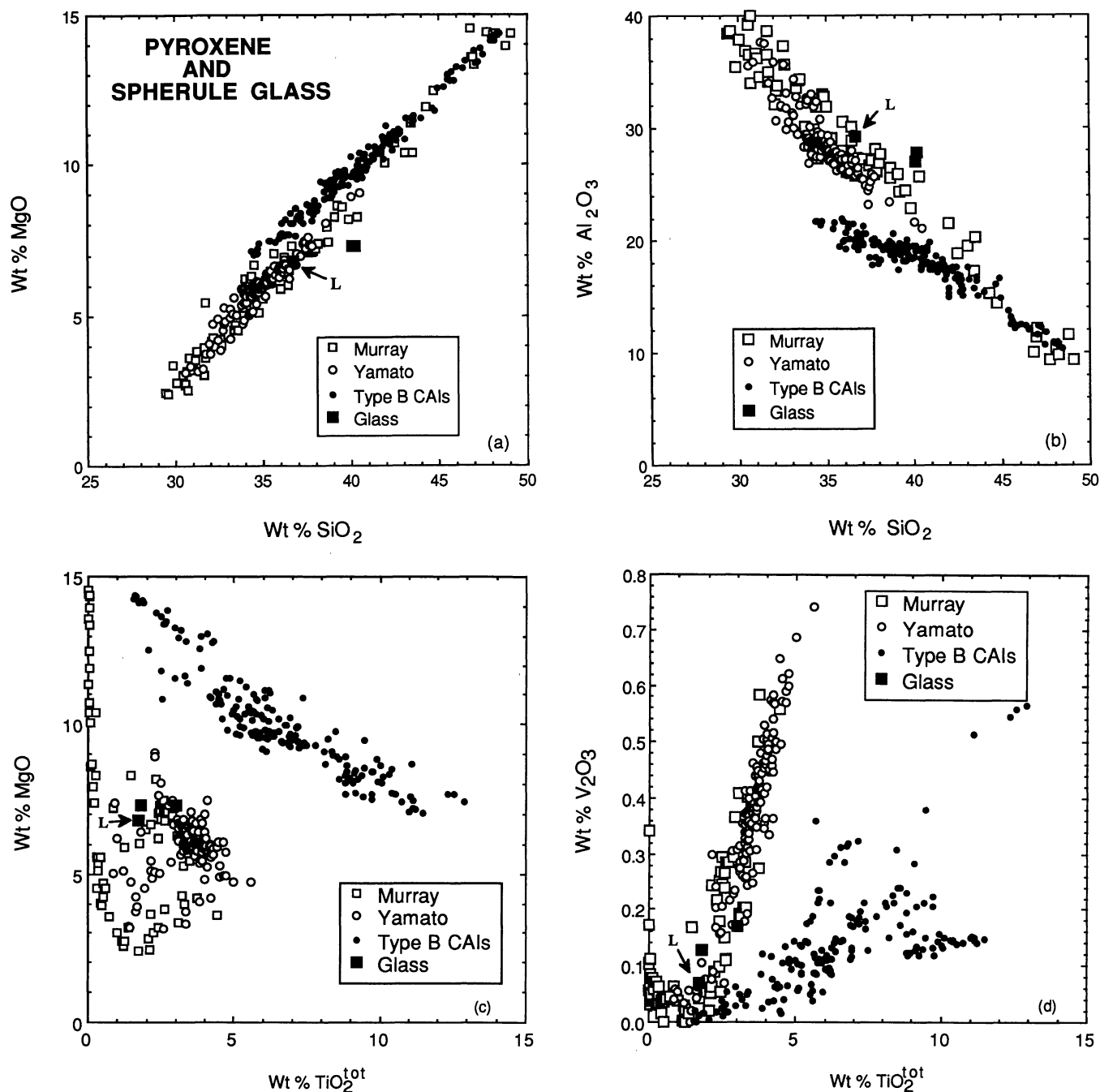


FIG. 5. Comparison of compositions of pyroxene in the spherules with those of fassaite from Allende Type B CAIs (Simon *et al.*, 1991) and with glass compositions from hibonite-glass spherules (Ireland *et al.*, 1991). The "L" indicates the glass in the spherule from Lancé. (a) MgO vs. SiO₂. (b) Al₂O₃ vs. SiO₂. (c) MgO vs. TiO₂^{tot}. (d) V₂O₃ vs. TiO₂^{tot}.

almost all other refractory inclusions. On the other hand, it may be that the relative D_s for Ti^{3+} and Ti^{4+} in the CaTs-rich pyroxene of the spherules are different from those of the fassaite from Type B inclusions. Kimura *et al.* (1993) analyzed a suite of refractory inclusions from the unique chondrite ALH 85085, some with extremely aluminous pyroxene (exceeding 80 mol% CaTs). They found no correlation between TiO₂ and Al₂O₃ in the aluminous pyroxene of these inclusions; therefore, it is unlikely that TiO₂ and MgO are anticorrelated in these pyroxenes. This is consistent with the

possibility that Ti partition coefficients for such aluminous pyroxenes are different from those for fassaite in Type B refractory inclusions.

In the spherules, TiO₂^{tot} is positively correlated with V₂O₃ (Fig. 5d), but more tightly than in the fassaite from Type B inclusions. The spherule pyroxene has higher V₂O₃/TiO₂^{tot} ratios than the Type B fassaite, possibly because, unlike the latter, the spherule pyroxene did not have to compete with spinel for V₂O₃.

Compositions of glass from hibonite-glass spherules are more similar to the compositions of spherule pyroxenes than to the Type B

fassaite compositions. The glass in the spherule from Lancé overlaps with the spherule pyroxene on all plots. In Fig. 5a,b, however, the other two glasses, which are both from Murchison spherules and have nearly identical compositions, plot slightly off the trends defined by the spherule pyroxene. In addition, the Murchison glasses have slightly lower CaO contents than the pyroxenes.

Hibonite—Representative analyses of hibonite from both spherules are given in Table 2. In both samples, hibonite has fairly low $\text{TiO}_2^{\text{tot}}$ and MgO contents; and individual grains have uniform compositions. The observed compositions are similar to those previously reported for hibonite in other hibonite-silicate spherules (Ireland *et al.*, 1991; Tomeoka *et al.*, 1992; Russell *et al.*, 1998). As illustrated in Fig. 6a, hibonite in Y17-6 generally has lower $\text{TiO}_2^{\text{tot}}$ contents (1.5–2.2 wt%) than that in MYSM3 (1.9–2.7 wt%) and has correspondingly lower MgO contents. The correlation of $\text{TiO}_2^{\text{tot}}$ and MgO, a common feature of meteoritic hibonite (e.g., Allen *et al.*, 1978; Beckett and Stolper, 1994), is due to the coupled substitution of $\text{Ti}^{4+} + \text{Mg}$ for 2Al. The minor amounts of Si found in meteoritic hibonite probably also substitute along with Mg for 2Al (Kornacki and Wood, 1985; Simon *et al.*, 1997b). A plot of Mg cations vs. (Ti + Si) cations in hibonite typically yields a trend with a slope of 1. On such a plot, Fig. 6b, analyses of the present samples have a slope of ~ 1 but do not plot along the 1:1 reference line. Most analyses have excess (Ti + Si) relative to Mg. This probably reflects the presence of Ti^{3+} , which can substitute directly for Al and is not coupled with Mg. If the observed excess (Ti + Si) is due to Ti^{3+} , then 10–20% of the Ti in the hibonite in the spherules is trivalent.

In comparing the two spherules considered here, we note that hibonite in Y17-6 has slightly lower $\text{TiO}_2^{\text{tot}}$ contents than that in MYSM3; while the pyroxene in the former has higher $\text{TiO}_2^{\text{tot}}$ contents than that in the latter.

Major Element Bulk Compositions—We calculated the major element bulk compositions of the spherules, normalized to 100%

TABLE 2. Electron microprobe analyses of hibonite.

	(1)	(2)	(3)	(4)
MgO	0.98	1.10	0.88	0.91
Al_2O_3	87.32	87.85	88.30	88.05
SiO_2	0.38	0.10	0.07	0.08
CaO	8.73	8.67	8.64	8.57
$\text{TiO}_2^{\text{tot}}$	1.99	2.46	1.89	2.04
Sc_2O_3	0.04	0.05	BLD	0.04
V_2O_3	BLD	0.04	BLD	0.03
FeO	0.03	BLD	0.12	0.24
Total	99.47	100.27	99.90	99.96
Cations per 19 oxygen anions				
Mg	0.165	0.183	0.147	0.152
Al	11.570	11.554	11.646	11.621
Si	0.043	0.011	0.008	0.009
Ca	1.052	1.036	1.036	1.028
Ti	0.168	0.206	0.159	0.172
Sc	0.002	0.005	0.0	0.002
V	0.0	0.004	0.0	0.001
Fe	0.003	0.0	0.012	0.023
Total cations	13.003	12.999	13.008	13.008

References: (1), (2) MYSM3. (3), (4) Y17-6.

BLD = below limit of detection of electron microprobe of 0.030 wt% for Sc_2O_3 , 0.022 wt% for V_2O_3 or 0.028 wt% for FeO.

$\text{MgO} + \text{Al}_2\text{O}_3 + \text{SiO}_2 + \text{CaO} + \text{TiO}_2^{\text{tot}}$, from their average pyroxene and hibonite compositions, and modal abundances converted to weight percent from volume percent using the phase densities. We assumed that the volume now occupied by nepheline in Y17-6 was originally pyroxene. The results are given in Table 3. The Yamato spherule has slightly more hibonite and a higher bulk Al_2O_3 content than MYSM3. The Yamato spherule is richer in $\text{TiO}_2^{\text{tot}}$ than the Murray spherule; while the latter is richer in MgO, SiO_2 and CaO than the former. The bulk composition of MYSM3 is similar to that of the glass-hibonite spherule from Lancé given by Ireland *et al.*

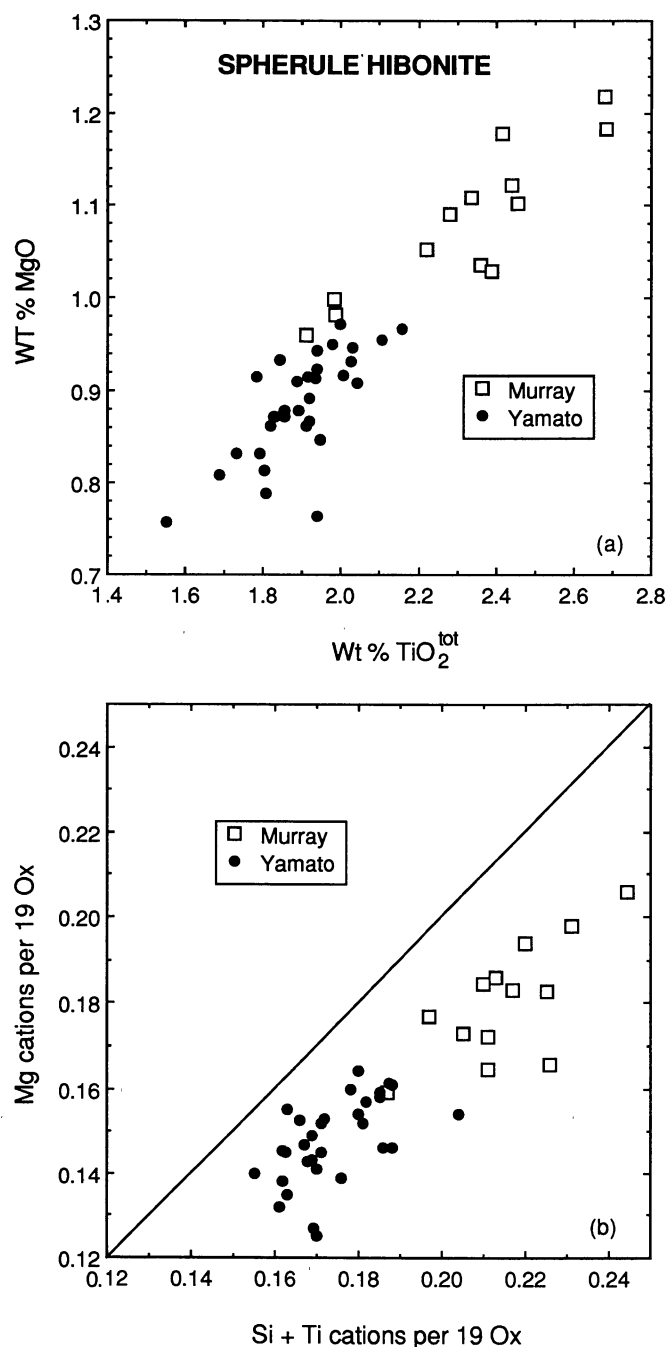


FIG. 6. Results of electron probe analyses of hibonite from the hibonite-pyroxene spherules. (a) MgO vs. $\text{TiO}_2^{\text{tot}}$. (b) Mg vs. Si + Ti, cations per 19 oxygen anions. A 1:1 correlation line is shown for reference.

TABLE 3. Modes, average mineral compositions, and bulk compositions of hibonite-pyroxene spherules.

	MYSM3			Y17-6		
	Hibonite	Pyroxene	Bulk	Hibonite	Pyroxene	Bulk
wt%	15.9	84.1		17.2	82.8	
No. of Analyses	13	79		33	136	
MgO	1.08	7.07	6.12	0.89	6.00	5.12
Al ₂ O ₃	87.68	27.91	37.41	88.33	29.10	39.27
SiO ₂	0.18	37.22	31.33	0.15	35.35	29.30
CaO	8.73	26.25	23.46	8.72	26.09	23.11
TiO ₂ ^{tot}	2.32	1.55	1.67	1.91	3.46	3.22

Densities used: Hibonite: 3.688 g/cc; Pyroxene: 3.30 g/cc.

(1991). The other hibonite-glass spherules from Murchison that were described by Ireland *et al.* (1991), however, have 28.9 and 47.0 wt% Al₂O₃, which are much lower and higher contents, respectively, than those found here.

Trace Element Abundances—Trace element abundances in both spherules were determined by ion microprobe mass spectrometry. Analyses are given in Table 4, and CI chondrite-normalized rare earth element (REE) abundances are illustrated in Fig. 7. The two patterns for MYSM3 pyroxene have positive slopes among the light REE (LREE), with La at $\sim 3 \times$ CI and Sm at $\sim 10 \times$ CI, negative Eu anomalies, and heavy REE (HREE) abundances from 10 to $30 \times$ CI.

We obtained one uncontaminated analysis of pyroxene in Y17-6 (no. 9), and it is quite similar to the analyses of pyroxene in MYSM3. It has low LREE abundances with a positive slope from La through Sm, a negative Eu anomaly, and HREE abundances that increase from Tb through Lu. Chondrite-normalized REE patterns of fassaite from Type B1 calcium-aluminum-rich inclusions (CAIs) are typically flat or have positive slopes with strong negative Eu anomalies (Simon *et al.*, 1991). The present patterns are generally similar to those, and the absolute abundances are at the lower end of the range observed by Simon *et al.* (1991). The fassaite-glass intergrowth analyzed by Russell *et al.* (1998) has much higher REE abundances, ~ 70 – $200 \times$ CI, than the present samples.

Hibonite in Y17-6 (no. 7) has flat REE abundances at ~ 50 – $60 \times$ CI for La through Dy, a negative Eu anomaly, and decreasing abundances of the HREE from Ho through Yb. This pattern is similar to those of most Murchison hibonites classified as PLACs by Ireland *et al.* (1988) as well as the hibonite in the spherule from Lancé (Ireland *et al.*, 1991) and in the spherules analyzed by Russell *et al.* (1998), although the latter hibonite has higher absolute REE abundances than the present samples.

Abundances of some of the other trace elements in the present samples exceed the ranges observed by Ireland *et al.* (1991) in hibonite-glass spherules. The Yamato spherule, with 135–227 ppm Sc in the pyroxene and 209 ppm in hibonite, has a much higher bulk Sc content (~ 190 ppm) than the spherules analyzed by Ireland *et al.* (1991), which have 27–42 ppm Sc. The abundances of Ba and Sr in the Yamato hibonite and fassaite are within the corresponding ranges of the hibonite and glass, respectively, in the hibonite-glass spherules (Ireland *et al.*, 1991).

An analysis of the nepheline in Y17-6 yielded a flat chondrite-normalized REE pattern with no Eu anomaly and abundances mostly between 10 and $20 \times$ CI. Abundances of Sr and Ba in the nepheline are $\sim 4 \times$ CI, which is much lower than is observed in melilite in coarse-grained CAIs (e.g., Kennedy *et al.*, 1997). Its low

Sr and Ba contents and lack of a positive Eu anomaly are consistent with formation of the nepheline from the aluminous pyroxene and make it unlikely that it was derived from melilite or anorthite, the more common precursors.

Isotopic Analyses—The isotopic compositions of Mg, Ca and Ti in both samples were determined by ion microprobe mass spectrometry. Results for Mg are given in Table 5 and illustrated in Fig. 8. In MYSM3, there is no significant isotopic mass fractionation of Mg; also, there is no resolvable excess ²⁶Mg in either the hibonite or the pyroxene. In contrast, in Y17-6, while the hibonite has $\Delta^{25}\text{Mg} \sim 0\text{‰}$ and no excess ²⁶Mg, the pyroxene has ²⁵Mg deficits, and ²⁶Mg ex-

TABLE 4. Major and trace element contents in hibonite-pyroxene spherules.

	MYSM3-4	MYSM3-5	Y17-6-7	Y17-6-9
MgO*	9.64	5.57	2.25	6.75
Al ₂ O ₃	20.5	30.5	79.2	26.7
SiO ₂	43.4	36.2	5.02	36.1
CaO	25.8	25.7	8.70	25.4
TiO ₂	0.43	1.71	2.00	3.22
FeO	0.06	0.03	2.20	1.07
Li	0.062 \pm 0.019	0.156 \pm 0.029	0.179 \pm 0.038	0.153 \pm 0.033
Be	0.787	0.847	2.59	0.335 \pm 0.047
B	1.11 \pm 0.18	1.07 \pm 0.17	1.84 \pm 0.25	1.39 \pm 0.21
F	39.0 \pm 8.9	75 \pm 12	35.0 \pm 9.0	50 \pm 10
Na	29.4	82.8	1970	1756
P	36.4 \pm 8.1	<33	134 \pm 18	89 \pm 13
Cl	68 \pm 34	251 \pm 61	99 \pm 44	124 \pm 47
K	30.1	73.0	429	377
Sc	34.9 \pm 6.3	130	209	227
Ti	2584	10234	11964	19331
V	272	677	281	2140
Cr	384	309	288	307
Mn	<34	<41	70.1 \pm 8.8	38 \pm 18
Fe	474 \pm 167	243 \pm 126	17108	8315
Co	6.5 \pm 3.6	9.1 \pm 3.6	43.3 \pm 5.8	25.9 \pm 4.7
Ni	<41	<37	943	419
Rb	0.50 \pm 0.39	1.14 \pm 0.41	1.83 \pm 0.66	3.68 \pm 0.71
Sr	51.4	26.8	77.4	30.1
Y	20.8	26.5	42.9	40.1
Zr	51.1	89.7	134	147
Nb	1.38 \pm 0.28	3.04 \pm 0.39	1.08 \pm 0.28	7.36
Cs	<0.27	0.48 \pm 0.24	0.35 \pm 0.25	<0.31
Ba	3.44 \pm 0.50	0.94 \pm 0.24	12.3	2.78 \pm 0.48
La	0.83 \pm 0.10	0.696 \pm 0.089	13.3	0.87 \pm 0.11
Ce	3.99	2.78 \pm 0.29	33.3	3.38 \pm 0.36
Pr	0.45 \pm 0.16	0.59 \pm 0.17	4.69 \pm 0.58	0.77 \pm 0.22
Nd	3.28 \pm 0.68	2.55 \pm 0.56	20.0	3.50 \pm 0.76
Sm	1.80 \pm 0.22	1.57 \pm 0.19	7.25 \pm 0.51	2.09 \pm 0.25
Eu	0.311 \pm 0.054	0.177 \pm 0.045	0.70 \pm 0.12	0.344 \pm 0.060
Gd	3.01 \pm 0.50	1.99 \pm 0.45	10.2 \pm 1.2	3.56 \pm 0.55
Tb	0.34 \pm 0.10	0.51 \pm 0.11	2.05 \pm 0.28	0.40 \pm 0.11
Dy	2.96 \pm 0.41	3.88 \pm 0.44	13.9	5.45 \pm 0.57
Ho	0.62 \pm 0.15	0.81 \pm 0.16	1.91 \pm 0.30	1.61 \pm 0.25
Er	2.69 \pm 0.31	3.90 \pm 0.34	3.57 \pm 0.44	5.34
Tm	0.276 \pm 0.065	0.668 \pm 0.092	0.203 \pm 0.068	1.16 \pm 0.14
Yb	1.72 \pm 0.34	2.90 \pm 0.39	0.46 \pm 0.39	5.41 \pm 0.58
Lu	0.74 \pm 0.12	0.44 \pm 0.10	<0.26	1.48 \pm 0.17
Th	0.37 \pm 0.11	0.41 \pm 0.11	1.47 \pm 0.26	0.205 \pm 0.091
U	0.096 \pm 0.055	0.141 \pm 0.063	0.137 \pm 0.079	0.32 \pm 0.11

*Oxide concentrations are given in wt% and element concentrations are given in parts per million. Uncertainties are $\pm 1\sigma$ and upper limits are $<2\sigma$, based on counting statistics. Uncertainties are only given when they exceed 10% (relative).

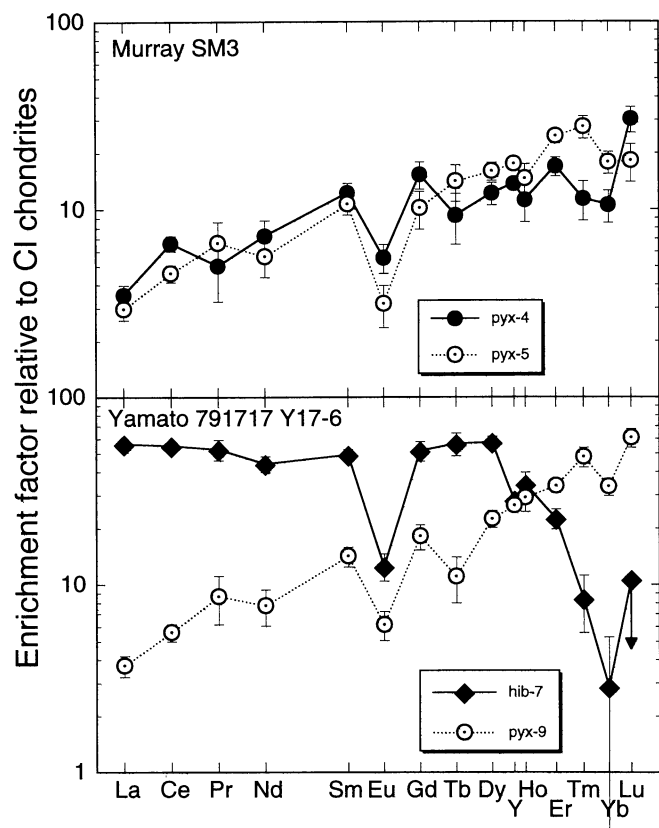


FIG. 7. The CI chondrite-normalized REE abundances in hibonite (hib) and pyroxene (pyx) in hibonite-pyroxene spherules.

cesses so large that they correspond to apparent initial $^{26}\text{Al}/^{27}\text{Al}$ ratios of $\sim 2\text{--}3 \times 10^{-4}$, which is much higher than the maximum value found in undisturbed refractory inclusions, 5×10^{-5} (MacPherson *et al.*, 1995). Large apparent initial $^{26}\text{Al}/^{27}\text{Al}$ ratios have been observed in disturbed CAIs and are generally attributed to redistribution of radiogenic ^{26}Mg from phases with high Al/Mg ratios to phases with low Al/Mg ratios. However, this is unlikely to have occurred *in situ* in Y17-6 because hibonite, the phase with the highest Al/Mg ratio in the spherule, has no radiogenic ^{26}Mg . Perhaps redistribution of ^{26}Mg occurred among the precursors of Y17-6. The present result is in sharp contrast with the ^{26}Mg deficits reported by Ireland *et al.* (1991) and Russell *et al.* (1998). The analyses of Y17-6 show that the hibonite and pyroxene in it are not in isotopic equilibrium.

Table 5. Magnesium isotopic compositions of hibonite-pyroxene spherules.

Sample	Phase	$^{27}\text{Al}/^{24}\text{Mg}$	$\Delta^{25}\text{Mg}$ (‰)	$\delta^{26}\text{Mg}$ (‰)
MYSM3	hib	44.8 ± 0.5	-2.7 ± 3.7	-0.3 ± 1.1
	hib	49.5 ± 0.2	-6.9 ± 3.7	2.6 ± 4.6
	pyx	7.7 ± 0.1	-3.0 ± 3.4	0.8 ± 3.4
Y17-6	hib	66.4 ± 2.0	5.6 ± 3.6	2.4 ± 4.2
	hib	86.6 ± 0.3	1.1 ± 2.4	1.6 ± 3.2
	hib, pyx	7.5 ± 2.6	-10.3 ± 2.6	8.4 ± 4.2
	pyx	10.8 ± 0.1	-3.4 ± 1.5	9.7 ± 2.5
	pyx	5.1 ± 0.0	-6.2 ± 1.5	12.7 ± 2.1
	pyx	4.7 ± 2.0	-3.8 ± 1.8	10.7 ± 2.5

Uncertainties are $\pm 2\sigma$.

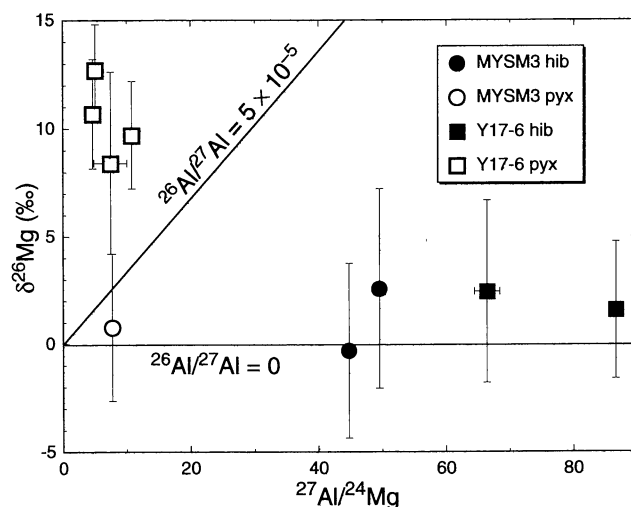


FIG. 8. The $\delta^{26}\text{Mg}$ vs. $^{27}\text{Al}/^{24}\text{Mg}$ for both hibonite-pyroxene spherules. Both phases in MYSM3 and hibonite in Y17-6 show no evidence of excess ^{26}Mg . Pyroxene in Y17-6 has large excesses of ^{26}Mg that, if representative of an undisturbed composition, would correspond to a very large initial $^{26}\text{Al}/^{27}\text{Al}$ ratio. Lines with slopes corresponding to initial $^{26}\text{Al}/^{27}\text{Al}$ ratios of 0 and 5×10^{-5} are shown for reference.

Another striking result of our analysis of these samples is the discovery of huge Ca and Ti isotopic anomalies. The data are given in Table 6 along with corrections for interferences from ^{48}Ti , ^{46}Ca , ^{50}V and ^{50}Cr . In each sample, analysis spot A sampled pyroxene and hibonite while spots B and C are almost completely in pyroxene. Despite this difference, the A analyses are within error of the B and C analyses for all isotopes measured, which suggests that within each spherule, the hibonite and the pyroxene that encloses it have similar Ca and Ti isotopic compositions. Sample Y17-6 is strongly depleted in ^{48}Ca and ^{50}Ti , and MYSM3 is enriched in these isotopes. The sizes of the ^{42}Ca and ^{43}Ca depletions in both spherules, as well as the ^{49}Ti depletion in Y17-6, are much smaller than the anomalies in the most neutron-rich isotopes.

Our results are compared to those for glassy hibonite-bearing spherules and coarse, platy hibonite crystals (the PLACs of Ireland *et al.*, 1988) in Fig. 9. The values of $\delta^{50}\text{Ti}$ reported here, $-61.4 \pm 4.1\%$ in Y17-6 and $103.4 \pm 5.2\%$ in MYSM3, are very close to the values of $-69 \pm 16\%$ (Y17-6) and $101 \pm 17\%$ (MYSM3) obtained from the trace element scans and previously reported by Simon *et al.* (1997a). These samples have two of the largest ^{50}Ti anomalies reported in CAIs to date (Hinton *et al.*, 1987; Ireland, 1988, 1990; Ireland *et al.*, 1988). As shown in Fig. 9, their isotopic compositions almost span the entire range found in the PLACs. In contrast, analyses of hibonite-glass spherules by Ireland *et al.* (1991) and Russell *et al.* (1998), shown in the open circles in Fig. 9, show no ^{50}Ti depletions and excesses of up to only $\sim 22\%$. Although they have much smaller ^{50}Ti excesses than does MYSM3, several hibonite-glass spherules have ^{48}Ca excesses comparable to that of MYSM3.

DISCUSSION

Predicted *versus* Texturally Inferred Crystallization Sequences

There are several ways to assess whether the hibonite grains found in the spherules crystallized in equilibrium with their hosts or are likely to be relict. If the hibonite had been dissolving in the melt at the time of solidification, we might expect the hibonite crystals to

Table 6. Calcium and Ti isotopic compositions of hibonite-pyroxene spherules and corrections for interferences in ‰.

	$\delta^{42}\text{Ca}$	$\delta^{43}\text{Ca}$	$\delta^{48}\text{Ca}$	$^{48}\text{Ti}_{\text{corr}}$			
Y17-6 Spot A	-10.8 ± 4.9	-7.0 ± 5.0	-46.8 ± 3.8	3.8			
Y17-6 Spot B	-8.1 ± 3.5	-4.1 ± 3.4	-45.6 ± 3.8	3.2			
Y17-6 Spot C	-6.5 ± 4.7	-4.9 ± 5.2	-39.4 ± 5.6	5.5			
Y17-6 average	-8.3 ± 2.4	-5.0 ± 2.5	-44.9 ± 2.4				
MYSM3 Spot A	-4.2 ± 3.5	-2.2 ± 4.9	34.4 ± 4.5	7.5			
MYSM3 Spot B	-7.0 ± 3.9	-3.7 ± 5.5	26.6 ± 4.5	11.7			
MYSM3 Spot C	-1.9 ± 8.2	-1.3 ± 7.0	38.5 ± 9.1	9.3			
MYSM3 average	-5.1 ± 2.5	-2.5 ± 3.2	31.4 ± 3.0				
	$\delta^{47}\text{Ti}$	$\delta^{49}\text{Ti}$	$\delta^{50}\text{Ti}$	$^{46}\text{Ca}_{\text{corr}}$	$^{50}\text{V}_{\text{corr}}$	$^{50}\text{Cr}_{\text{corr}}$	
Y17-6 Spot A	0.4 ± 5.4	-13.0 ± 5.1	-63.7 ± 6.2	10.1	1.3	6.0	
Y17-6 Spot B	-3.7 ± 5.9	-8.4 ± 6.3	-58.7 ± 7.0	12.7	1.3	7.0	
Y17-6 Spot C	5.2 ± 7.2	-12.8 ± 7.8	-61.2 ± 8.5	12.7	1.3	7.3	
Y17-6 average	0.1 ± 3.5	-11.5 ± 3.5	-61.4 ± 4.1				
MYSM3 Spot A	-2.2 ± 5.2	3.1 ± 5.5	103.6 ± 7.8	16.5	1.2	9.0	
MYSM3 Spot B	-1.0 ± 5.4	-0.6 ± 6.0	100.1 ± 8.2	14.7	1.3	8.5	
MYSM3 Spot C	2.2 ± 8.3	8.1 ± 8.5	112.5 ± 14.1	25.1	0.8	17.5	
MYSM3 average	-1.0 ± 3.4	2.7 ± 5.4	103.4 ± 5.2				

Averages are weighted means. Uncertainties are $\pm 2\sigma$.

Instrumental mass fractionation on Madagascar hibonite: $F_{\text{Ca}} = -5.2 \pm 1.3 \text{ ‰/amu}$; $F_{\text{Ti}} = -18.9 \pm 1.9 \text{ ‰/amu}$.

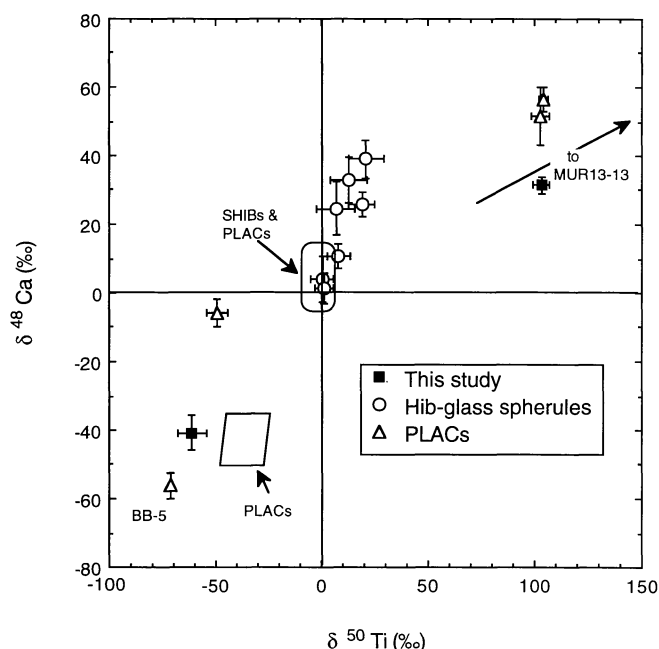


FIG. 9. Plot of $\delta^{48}\text{Ca}$ vs. $\delta^{50}\text{Ti}$ in hibonite-pyroxene spherules (this study), hibonite-glass spherules (Ireland *et al.*, 1991; Russell *et al.*, 1998), and in hibonite from other inclusions in Murchison and Murray. Fields for typical platy hibonite crystals (PLACs) and spinel-hibonite inclusions (SHIBs) after Ireland (1990) and Ireland *et al.* (1991). Data for anomalous PLACs (open triangles) from Zinner *et al.* (1986) and Fahey *et al.* (1987).

appear somewhat embayed or rounded. We can also look for chemical gradients in the host that would be consistent with hibonite dissolution, such as increasing Al_2O_3 and decreasing SiO_2 contents with decreasing distance from hibonite. We can use known phase relations to assess whether hibonite would be expected to crystallize stably from melts with the bulk compositions of the spherules. In

addition, we can estimate hibonite/liquid Ds from the samples. Distribution coefficients that are in the range of experimentally determined values would suggest that the hibonite crystallized stably and *in situ*, as would evidence for isotopic equilibrium between hibonite and pyroxene.

Spherule MYSM3—To predict their equilibrium crystallization sequences, we projected the bulk compositions of the spherules onto two composition planes of the appropriate phase equilibria. When projected from spinel onto the gehlenite-anorthite-forsterite plane of the $\text{CaO-MgO-Al}_2\text{O}_3\text{-SiO}_2$ (CMAS) system (Fig. 10), we find that the composition of MYSM3 is spinel-saturated and projects into the anorthite field (Stolper, 1982). As indicated by the arrow from the data point in Fig. 10, upon crystallization of anorthite, the composition of the residual liquid will move directly away from the anorthite apex and toward the anorthite-melilite join. Spinel + anorthite should be joined by melilite and then possibly by pyroxene at the eutectic. Projecting the composition from hibonite onto the gehlenite-anorthite-spinel plane of the same system, we find that it plots well below the hibonite saturation surface of Beckett and Stolper (1994) by $\sim 25 \text{ wt\%}$ hibonite. This suggests that, at equilibrium, hibonite should not crystallize early. The observed textural relationship of hibonite enclosed in pyroxene is, in contrast, consistent with early crystallization of hibonite, followed by pyroxene. Because several of the plates have ragged ends and because hibonite is not a member of the equilibrium crystallization sequence, it is most likely relict. Ratios of $(\text{TiO}_2^{\text{tot}} \text{ in hibonite})/(\text{bulk TiO}_2^{\text{tot}})$ ranging from 1.2–1.6, however, are well within the range (0.8–2.0) of experimentally determined hibonite/liquid Ds (Beckett and Stolper, 1994; Kennedy *et al.*, 1994). The hibonite in this spherule could be relict but perhaps crystallized originally from a liquid with a $\text{TiO}_2^{\text{tot}}$ content similar to that of MYSM3. A similar situation exists for MUR7-228, a hibonite-glass spherule from Murchison, first described by Ireland *et al.* (1991). The bulk composition of this spherule plots well outside of the hibonite stability field (Beckett and Stolper, 1994), yet its hibonite/glass Ds for Ti and trace ele-

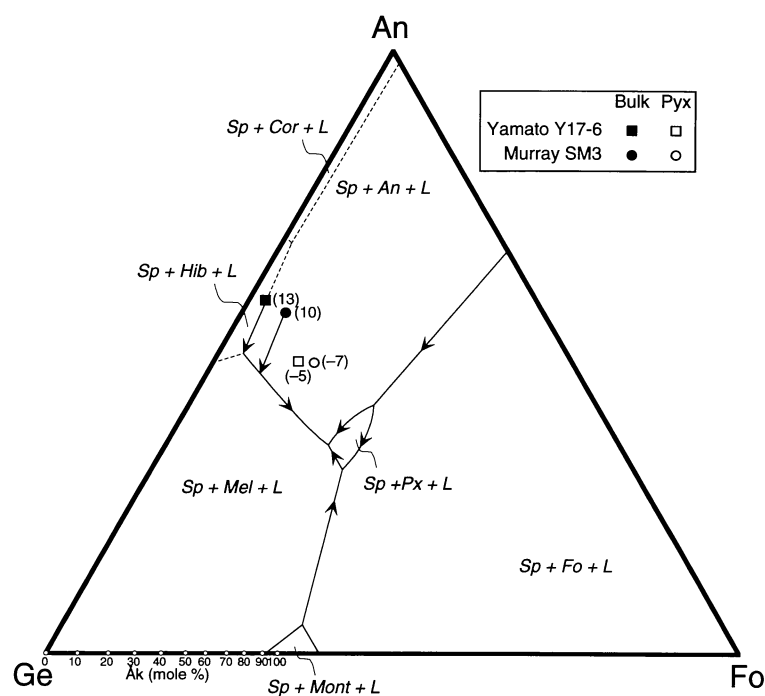


FIG. 10. Projection of bulk spherule and average pyroxene compositions, in wt%, from spinel onto the gehlenite-anorthite-forsterite plane of the CMAS system. The predicted trends of residual liquid composition during equilibrium crystallization are indicated by the arrows extending away from the spherule compositions to the anorthite-melilite cotectic. The spinel coordinates for the pyroxene compositions are given in parentheses. Phase equilibria after Stolper (1982).

ments are similar to experimentally determined values (Ireland *et al.*, 1991). Beckett and Stolper (1994) suggested that the results for MUR7-228 could reflect *in situ*, metastable crystallization of hibonite that nucleated on relict cores, with the thin section sampling only the overgrowths. Alternatively, Beckett and Stolper (1994) also suggested that the thin section could have undersampled hibonite and that hibonite could have crystallized stably from the true bulk composition. Neither of these scenarios can be completely ruled out for MYSM3.

The pyroxene appears to have crystallized *in situ* around the hibonite but is so CaTs-rich that it probably crystallized metastably. Its presence is discussed below.

Spherule Y17-6—In the CMAS system, the bulk composition of Y17-6, like that of MYSM3, is spinel-saturated. When projected from spinel (Fig. 10), the composition of Y17-6 falls on the anorthite-hibonite cotectic. As indicated on the diagram, these phases should be joined in the crystallization sequence by melilite. When projected from hibonite, the spherule composition plots below the hibonite saturation surface of Beckett and Stolper (1994), which also indicates that hibonite is not the liquidus phase. The equilibrium sequence (in which spinel is first, then followed by anorthite and hibonite and is joined then by melilite) consists mostly of phases that are not found in the sample and contrasts with the texturally inferred sequence of hibonite followed by pyroxene.

Petrographically, the hibonite crystals in Y17-6 are not embayed, but some are rounded, possibly reflecting partial dissolution. Although we did not detect any chemical gradients adjacent to the observed hibonite, the most Al-rich, Ti-poor pyroxene in this sample may have formed as a result of local Al-enrichment of the melt

due to dissolution of hibonite. In the chemical trends illustrated in Fig. 4, as Al_2O_3 decreases, the other major pyroxene components, Di and Tpx, both increase despite the fact that these two components are normally anticorrelated, as they are in the central part of the traverse. The trends in the traverse can best be explained by crystallization after a local increase in the Al_2O_3 content of the liquid. This resulted in a sharp increase in the Al_2O_3 content of the pyroxene with increasing crystallization, a reversal of the trend seen in typical Type B fassaite. Because these are essentially Mg-Al pyroxenes, this forced a complementary reversal of the typical MgO trend, causing MgO to decrease with crystallization and to correlate with $\text{TiO}_2^{\text{tot}}$. Spinel is not a good candidate for the phase that dissolved because, in addition to Al_2O_3 , it would contribute MgO to the melt, and MgO enrichment is not associated with the Al_2O_3 enrichment.

For this spherule, the calculated distribution coefficients for Ti in hibonite, based on hibonite/bulk ratios, are mostly between 0.5 and 0.7, which are slightly lower than the experimentally determined range. The trace element abundances are also roughly consistent with equilibrium partitioning. For example, our ion probe analyses show that pyroxene has a La content of $3.7 \times \text{CI}$, and hibonite has $56.5 \times \text{CI}$. From the proportions of the phases given in Table 3, we calculate a bulk La content of $\sim 13 \times \text{CI}$, giving a ratio of La in hibonite/bulk La of ~ 4.4 , which is close to the hibonite/liquid Ds of 5–6 reported by Kennedy *et al.* (1994). Although the mineral chemistry of Y17-6 does not rule out an *in situ* origin of the hibonite, the Mg isotopic analyses (Table 5) strongly indicate that the pyroxene and hibonite in Y17-6 are not in equilibrium; the fassaite in this sample has a deficit in ^{25}Mg and excess ^{26}Mg but the hibonite has neither. The isotopic data are not consistent with the hibonite and pyroxene having the same initial $^{26}\text{Al}/^{27}\text{Al}$ ratio.

Crystallization of CaTs-rich Pyroxene

In fassaite from Type B inclusions, Mg and Si are strongly correlated and enriched in late relative to early pyroxene; while Al and Si are strongly anticorrelated (Simon *et al.*, 1991). The same Mg-Si-Al relationships are observed in the spherule pyroxene as well (Fig. 5a,b), which suggests that it, too, crystallized from a liquid. The trace element data are also consistent with crystallization of the spherule pyroxenes from melts. The chondrite-normalized REE patterns of the pyroxene are like those of igneous fassaite from Type B inclusions (Simon *et al.*, 1991).

Pyroxenes as aluminous as those in the spherules probably are very rare because these compositions are unstable relative to the assemblage spinel + anorthite. In a series of isothermal, equilibrium experiments at near-liquidus conditions in the Di-CaTs-Tpx system, Yang (1975) synthesized Al-, Ti^{4+} -bearing clinopyroxene and determined its stability field. The maximum amount of CaTs component found in his synthetic pyroxene is $\sim 23 \text{ mol}\%$. In Type B refractory inclusions, fassaite averages $\sim 25 \text{ mol}\%$ CaTs (Beckett, 1986), and contents up to $\sim 30 \text{ mol}\%$ have been observed (Simon *et al.*, 1991). All the pyroxene in the spherules, with the exception of the extremely Di-rich pyroxene in MYSM3, has between 40 and 80 $\text{mol}\%$ CaTs; however, it is all too CaTs-rich to plot within the field of Al-, Ti-bearing pyroxene of Yang (1975).

If we assume that the hibonite in the spherules is relict and the host liquid crystallized completely to the enclosing pyroxene, then the average pyroxene compositions should represent the compositions of the host liquids. To determine whether or not these compositions are spinel-saturated, we projected them from spinel onto the gehlenite-anorthite-forsterite plane of the CMAS system (Fig. 10) to see where they plot relative to the spinel saturation surface of Stolper (1982). The results show that they are slightly undersaturated in spinel and plot within the field of primary anorthite crystallization. Assuming that no other stability field intervenes and that anorthite should have crystallized first, then its absence and that of spinel are easily explained. Experiments by MacPherson *et al.* (1984) showed that, in melts with the compositions of Type B inclusions, anorthite crystallization is suppressed relative to pyroxene at cooling rates as low as 0.5 °C/h. This is believed to indicate that melilite crystallization continues, even after the liquid composition enters the anorthite field, until a metastable extension of the pyroxene field is encountered (MacPherson *et al.*, 1984). The spherule liquids probably started in the anorthite field and did not crystallize at all until the pyroxene field was encountered. A high or even moderate cooling rate, a liquid with pyroxene stoichiometry, and perhaps pyroxene nuclei could have caused metastable crystallization of pyroxene, rather than crystallization of anorthite or quenching of the liquid to a glass. The lack of any prior crystallization of aluminous phases that should have crystallized might account for the extraordinarily high CaTs contents of the spherule pyroxene. It is worth noting that Beckett and Stolper (1994) cooled a hibonite-saturated melt at 5 °C/h and found that, like the present samples, it did not follow its equilibrium crystallization sequence. In that run, hibonite crystallized first, as expected, but it was followed by melilite, UNK (a Ti-rich phase found in some CAIs), and pyroxene with ~50 mol% CaTs, instead of spinel and grossite. We agree with the conclusions of Beckett and Stolper (1994) that the cooling rate of this run, although not extremely fast, was rapid enough that phases that should have been stable did not nucleate and that this effect could account for the occurrence of hibonite + CaTs-rich pyroxene in spherules. Kimura *et al.* (1993) also concluded that the extremely aluminous pyroxene they found had crystallized metastably.

Glass compositions in the hibonite-glass spherules (Ireland *et al.*, 1991) are generally similar to typical pyroxene compositions in the hibonite-pyroxene spherules; so, the glass-bearing spherules probably cooled at least as fast as the pyroxene-bearing ones. It is not known, however, how fast such a melt would have to be cooled either to be quenched to a glass or to crystallize pyroxene metastably. Reid *et al.* (1974) found a glassy chondrule in Vigarano and attempted to quench to a glass a synthetic melt of the chondrule composition: ~22 wt% SiO₂, 40% Al₂O₃, 13% MgO, and 25% CaO. This composition is more SiO₂-poor than those of the spherules; yet, even when cooled from 1800 °C to room temperature in <30 s (*i.e.*, ~60 °C/s), the run product was not glassy and was thought to consist of fine-grained spinel + melilite. Even faster cooling rates have been inferred for a crystalline, spinel-, grossite-bearing inclusion from Murchison (Simon *et al.*, 1994). It is possible that the hibonite-pyroxene spherules cooled at much more moderate rates. If all that is required in the present case is suppression of anorthite crystallization relative to pyroxene, then the hibonite-pyroxene spherules could have cooled at rates similar to those inferred for Type B inclusions. It is also possible that glass-bearing and pyroxene-bearing spherules cooled at similar rates but the latter

had pyroxene nuclei present in the melts, causing pyroxene to nucleate within the spherules and grow outward upon cooling, rather than nucleating on the spherule edges or being quenched to a glass.

Are All Hibonite-Silicate Spherules Genetically Related?

The present results, with ⁴⁸Ca and ⁵⁰Ti enriched in one sample and depleted in the other, are consistent with nucleosynthesis models in which these isotopes are cogenetic (Hartmann *et al.*, 1985; Meyer *et al.*, 1996). This would lead to the existence of grains enriched in both isotopes, like the precursors of MYSM3, and grains with low proportions of those isotopes, like the precursors of Y17-6. Workers who have studied the glassy hibonite-silicate spherules concluded that they all formed from an isotopic reservoir that was enriched in ⁴⁸Ca and ⁵⁰Ti and lacked ²⁶Al (Ireland *et al.*, 1991; Russell *et al.*, 1998). The Murray sample could be from such a reservoir, though it has by far a much greater ⁵⁰Ti excess than reported for the other spherules. The Yamato sample, however, could not have formed in such a reservoir and, therefore, it is not genetically related to the other spherules. Unlike all of the other hibonite-silicate spherules, it is strongly depleted in ⁴⁸Ca and ⁵⁰Ti, and its pyroxene contains excess ²⁶Mg while its hibonite does not.

There are two possible interpretations of the Mg isotopic compositions in Y17-6. (1) Pyroxene in Y17-6 has low Al/Mg ratios with $\delta^{26}\text{Mg}$ values of ~+10‰, giving an apparent initial ²⁶Al/²⁷Al ratio of 2–3 × 10⁻⁴. Given the large ⁵⁰Ti anomaly and ²⁵Mg deficit in this spherule, one must consider the possibility that this object has nucleosynthetic Mg isotopic anomalies not necessarily related to the decay of ²⁶Al. In this regard, the hibonite and pyroxene apparently do not have the same Mg isotopic anomaly but do appear to have the same anomalous Ca and Ti isotopic composition. (2) If the ²⁶Mg anomalies are due to ²⁶Al decay with no later redistribution of Mg, two reservoirs are required for the formation of Y17-6: one ²⁶Al-free (hibonite) and one ²⁶Al-rich (molten precursors), with the latter reservoir having an ²⁶Al/²⁷Al ratio ~5× the ratio found in any other undisturbed CAI so far studied (MacPherson *et al.*, 1995). The presence of hibonite with no excess ²⁶Mg implies that the hibonite either formed prior to addition of ²⁶Al to the solar nebula or that the distribution of ²⁶Al was heterogeneous and ²⁶Al-free reservoirs persisted after addition of ²⁶Al to the solar nebula. It is unlikely that the hibonite in Y17-6 formed after the complete decay of ²⁶Al to ²⁶Mg and then was enclosed in a liquid containing live ²⁶Al. This would require a second addition of ²⁶Al to the solar nebula, which would be inconsistent with the recognition of a single dominant ²⁶Al/²⁷Al ratio of 5 × 10⁻⁵ (MacPherson *et al.*, 1995). Another problem with this scenario is that both pyroxene and hibonite in Y17-6 show anomalously large deficits in ⁴⁸Ca and ⁵⁰Ti, which argues against their being brought together by random capture.

The distinctive isotopic compositions of the present samples indicate that they are not related to each other, and it is unlikely that they are related to any of the previously described hibonite-silicate spherules. The glass-bearing and the glass-free, pyroxene-bearing spherules, therefore, do not simply represent materials from a single isotopic reservoir that were cooled at different rates. We conclude that they represent materials from different sources.

The present results somewhat weaken the arguments of Ireland *et al.* (1991) against derivation of the PLACs from spherules, based on isotopic and trace element differences. The Ca and Ti isotopic compositions of MYSM3 and Y17-6, and presumably the hibonite they contain, nearly span the wide range of compositions exhibited by the PLACs. Also, the low Mg and Ti concentrations in hibonite

of both spherules, as well as the chondrite-normalized abundance pattern of REE and other trace elements of the hibonite in Y17-6, are similar to those of several PLACs analyzed by Ireland (1990). A serious problem with derivation of PLACs from spherules that was pointed out by Ireland *et al.* (1991) remains: most PLACs are fragments of once-larger crystals, yet they are still much larger than the hibonite grains found in spherules. It still seems unlikely that PLACs were derived from spherules.

CONCLUSIONS

Both spherules formed by solidification of melts. Beckett and Stolper (1994) showed that a likely precursor phase assemblage for hibonite-glass spherules is spinel + hibonite + melilite. From our results and observations, we conclude that the present samples contain relict hibonite, implying that hibonite was also present among the precursor grains that melted to form the hibonite-pyroxene spherules. The heating events that formed the melts were too brief and/or not hot enough to melt all the hibonite. The droplets cooled quickly enough that extremely aluminous pyroxene crystallized metastably instead of anorthite. The Mg-Si-Al relationships in the spherule pyroxenes are similar to those observed in fassaite from Type B inclusions; but in contrast with typical fassaite, we do not observe an anticorrelation between MgO and $\text{TiO}_2^{\text{tot}}$ in the spherule pyroxene. This may mean that the aluminous pyroxene of the spherules has different relative distribution coefficients for Ti^{3+} and Ti^{4+} from those found for fassaite in Type B inclusions.

The precursor grains of the two spherules considered here did not form in the same isotopic reservoir. One spherule, MYSM3, has large excesses of ^{48}Ca and ^{50}Ti and no excess ^{26}Mg ; while the other spherule, Y17-6, has large deficits of ^{48}Ca and ^{50}Ti and excess ^{26}Mg in its pyroxene. These results, especially for the latter sample, contrast with those for hibonite-, glass-bearing spherules for which no excess ^{26}Mg and slight excesses of ^{50}Ti have been reported (Ireland *et al.*, 1991; Russell *et al.*, 1998). Although they are rare and texturally similar to each other, hibonite-silicate spherules are not all from the same source, having sampled at least two different isotopic reservoirs, attesting to the heterogeneity of the early solar nebula.

Acknowledgments—We are very grateful to A. Hsu and P. Sylvester for performing the disaggregation and density separation, respectively, of the Murray sample; to the Field Museum of Natural History for the loan of the Murray sample; to K. Tomeoka (Kobe University) and H. Kojima (NIPR, Japan) for their prompt response to our request for a loan of the Yamato sample; and to S. Russell for kindly providing a preprint. Discussions with J. R. Beckett were helpful as were reviews by A. El Goresy and T. Ireland. This work was supported by the National Aeronautics and Space Administration through grants NAGW-3340 and NAG5-4476 (LG), NAGW-3384 and NAG5-4298 (AMD), NAG5-4493 (EKZ), and NAGW-3345 (to R. N. Clayton), and funding is gratefully acknowledged.

Editorial handling: D. W. G. Sears

REFERENCES

- ALLEN J. M., GROSSMAN L., DAVIS A. M. AND HUTCHEON I. D. (1978) Mineralogy, textures and mode of formation of a hibonite-bearing Allende inclusion. *Proc. Lunar Planet. Sci. Conf.* **9th**, 1209–1233.
- BECKETT J. R. (1986) The origin of calcium-, aluminum-rich inclusions from carbonaceous chondrites: An experimental study. Ph.D. thesis, Univ. of Chicago. 373 pp.
- BECKETT J. R. AND STOLPER E. (1994) The stability of hibonite, melilite and other aluminous phases in silicate melts: Implications for the origin of hibonite-bearing inclusions from carbonaceous chondrites. *Meteoritics* **29**, 41–65.
- FAHEY A. J., GOSWAMI J. N., MCKEEGAN K. D. AND ZINNER E. K. (1987) ^{16}O excesses in Murchison and Murray hibonites: A case against a late supernova injection origin of isotopic anomalies in O, Mg, Ca, and Ti. *Astrophys. J.* **323**, L91–L95.
- GROSSMAN J. N., RUBIN A. E. AND MACPHERSON G. J. (1988) ALH 85085: A unique volatile-poor carbonaceous chondrite with possible implications for nebular fractionation processes. *Earth Planet. Sci. Lett.* **91**, 33–54.
- HARTMANN D., WOOSLEY S. E. AND EL EID M. F. (1985) Nucleosynthesis in neutron-rich supernova ejecta. *Astrophys. J.* **297**, 837–845.
- HINTON R. W., DAVIS A. M. AND SCATENA-WACHEL D. E. (1987) Large negative ^{50}Ti anomalies in refractory inclusions from the Murchison carbonaceous chondrite—Evidence for incomplete mixing of neutron-rich supernova ejecta into the solar system. *Astrophys. J.* **313**, 420–428.
- IRELAND T. R. (1988) Correlated morphological, chemical, and isotopic characteristics of hibonites from the Murchison carbonaceous chondrite. *Geochim. Cosmochim. Acta* **52**, 2827–2839.
- IRELAND T. R. (1990) Presolar isotopic and chemical signatures in hibonite-bearing refractory inclusions from the Murchison carbonaceous chondrite. *Geochim. Cosmochim. Acta* **54**, 3219–3237.
- IRELAND T. R., FAHEY A. J. AND ZINNER E. K. (1988) Trace-element abundances in hibonites from Murchison carbonaceous chondrite: Constraints on high temperature processes in the solar nebula. *Geochim. Cosmochim. Acta* **52**, 2841–2854.
- IRELAND T. R., FAHEY A. J. AND ZINNER E. K. (1991) Hibonite-bearing microspherules: A new type of refractory inclusions with large isotopic anomalies. *Geochim. Cosmochim. Acta* **55**, 367–379.
- KENNEDY A. K., LOFGREN G. E. AND WASSERBURG G. J. (1994) Trace-element partition coefficients for perovskite and hibonite in meteorite compositions. *Chem. Geol.* **117**, 379–390.
- KENNEDY A. K., BECKETT J. R., EDWARDS D. A. AND HUTCHEON I. D. (1997) Trace element disequilibria and magnesium isotope heterogeneity in 3655A: Evidence for a complex multi-stage evolution of a typical Allende type B1 CAI. *Geochim. Cosmochim. Acta* **61**, 1541–1561.
- KIMURA M., EL GORESY A., PALME H. AND ZINNER E. (1993) Ca-, Al-rich inclusions in the unique chondrite ALH 85085: Petrology, chemistry, and isotopic compositions. *Geochim. Cosmochim. Acta* **57**, 2329–2359.
- KORNACKI A. S. AND WOOD J. A. (1985) Mineral chemistry and origin of spinel-rich inclusions in the Allende CV3 chondrite. *Geochim. Cosmochim. Acta* **49**, 1219–1237.
- KURAT G. (1975) Der kohlige Chondrit Lancé: Eine petrologische Analyse der komplexen Genese eines Chondriten. *Tschermaks Mineral. Petrogr.* **22**, 38–78.
- MACDOUGALL J. D. (1981) Refractory spherules in the Murchison meteorite: Are they chondrules? *Geophys. Res. Lett.* **8**, 966–969.
- MACPHERSON G. J. AND DAVIS A. M. (1993) A petrologic and ion microprobe study of a Vigarano Type B refractory inclusion: Evolution by multiple stages of alteration and melting. *Geochim. Cosmochim. Acta* **57**, 231–243.
- MACPHERSON G. J. AND DAVIS A. M. (1994) Refractory inclusions in the prototypical CM chondrite, Mighei. *Geochim. Cosmochim. Acta* **58**, 5599–5625.
- MACPHERSON G. J., BAR-MATTHEWS M., TANAKA T., OLSEN E. AND GROSSMAN L. (1980) Refractory inclusions in Murchison: Recovery and mineralogical description (abstract). *Lunar Planet. Sci.* **11**, 660–662.
- MACPHERSON G. J., BAR-MATTHEWS M., TANAKA T., OLSEN E. AND GROSSMAN L. (1983) Refractory inclusions in the Murchison meteorite. *Geochim. Cosmochim. Acta* **47**, 823–839.
- MACPHERSON G. J., PAQUE J. M., STOLPER E. AND GROSSMAN L. (1984) The origin and significance of reverse zoning in melilite from Allende Type B inclusions. *J. Geol.* **92**, 289–305.
- MACPHERSON G. J., DAVIS A. M. AND GROSSMAN J. N. (1989) Refractory inclusions in the unique chondrite ALH 85085 (abstract). *Meteoritics* **24**, 297.
- MACPHERSON G. J., DAVIS A. M. AND ZINNER E. K. (1995) The distribution of ^{26}Al in the early solar system—A reappraisal. *Meteoritics* **30**, 365–386.
- MEYER B. S., KRISHNAN T. D. AND CLAYTON D. D. (1996) ^{48}Ca production in matter expanding from high temperature and density. *Astrophysics J.* **462**, 825–838.
- POUCHOU J. L. AND PICHOU F. (1984) A new model for quantitative x-ray microanalysis. Part I: Application to the analysis of homogeneous samples. *Rech. Aerosp.* **1984–3**, 13–38.
- REID A. M., WILLIAMS R. J., GIBSON E. K., JR. AND FREDRIKSSON K. (1974) A refractory glass chondrule in the Vigarano chondrite. *Meteoritics* **9**, 35–45.

- RUSSELL S. S., HUSS G. R., FAHEY A. J., GREENWOOD R. C., HUTCHISON R. AND WASSERBURG G. J. (1998) An isotopic and petrologic study of calcium-aluminum-rich inclusions from CO3 meteorites. *Geochim. Cosmochim. Acta* **62**, 689–714.
- SIMON S. B., GROSSMAN L., AND DAVIS A. M. (1991) Fassaite composition trends during crystallization of Allende Type B refractory inclusion melts. *Geochim. Cosmochim. Acta* **55**, 2635–2655.
- SIMON S. B., GROSSMAN L. AND HSU A. (1993) Petrography and origin of refractory inclusions from the Murray and Murchison C2 chondrites (abstract). *Lunar Planet. Sci.* **24**, 1309–1310.
- SIMON S. B., YONEDA S., GROSSMAN L. AND DAVIS A. M. (1994) A CaAl_4O_7 -bearing refractory spherule from Murchison: Evidence for very high-temperature melting in the solar nebula. *Geochim. Cosmochim. Acta* **58**, 1937–1949.
- SIMON S. B., DAVIS A. M. AND GROSSMAN L. (1997a) Hibonite-bearing spherules with extremely aluminous pyroxene and large titanium-50 anomalies (abstract). *Meteorit. Planet. Sci.* **32** (Suppl.), A121–A122.
- SIMON S. B., GROSSMAN L. AND DAVIS A. M. (1997b) Multiple generations of hibonite in spinel-hibonite inclusions from Murchison. *Meteorit. Planet. Sci.* **32**, 259–269.
- STOLPER E. (1982) Crystallization sequences of Ca-Al-rich inclusions from Allende: An experimental study. *Geochim. Cosmochim. Acta* **46**, 2159–2180.
- TOMEOKA K., NOMURA K. AND TAKEDA H. (1992) Na-bearing Ca-Al-rich inclusions in the Yamato 791717 CO carbonaceous chondrite. *Meteoritics* **27**, 136–143.
- YANG H.-Y. (1975) Al- and Ti-rich clinopyroxene in the system $\text{CaMg-Si}_2\text{O}_6\text{-CaAl}_2\text{SiO}_6\text{-CaTiAl}_2\text{O}_6$. *Proc. Geol. Soc. China* **18**, 48–58.
- YONEDA S. AND GROSSMAN L. (1995) Condensation of $\text{CaO-MgO-Al}_2\text{O}_3\text{-SiO}_2$ liquids from cosmic gases. *Geochim. Cosmochim. Acta* **59**, 3413–3444.
- ZINNER E. K., FAHEY A. J., GOSWAMI J. N., IRELAND T. R. AND MCKEEGAN K. D. (1986) Large ^{48}Ca anomalies are associated with ^{50}Ti anomalies in Murchison and Murray hibonites. *Astrophys. J.* **311**, L103–L107.